IEEE Access
Multidisciplinary ⋮ Rapid Review ⋮ Open Access Journal

Received November 20, 2021, accepted December 20, 2021, date of publication December 24, 2021,
date of current version December 31, 2021.

Digital Object Identifier 10.1109/ACCESS.2021.3138698

Series-Fed Monopulse Microstrip Array Antenna With Stripline Quadrature Hybrid Comparator Network

LE ZOU[1], XUETIAN WANG[1], AND JIAWEI ZANG[2], (Member, IEEE)
[1]School of Information and Electronics, Beijing Institute of Technology, Beijing 100081, China
[2]China Academy of Information and Communications Technology, Beijing 100191, China

Corresponding author: Jiawei Zang (zangjiawei@caict.ac.cn)

ABSTRACT Microstrip series-fed weighted arrays have widespread applications in millimeter wave (MMW) radar due to their low profile and light weight. Our study proposes a novel Ka-band compact monopulse radar antenna design with a highly directional 2D series-fed microstrip array antenna. The structure is composed of a symmetrical four quadrant radiation array and an innovative stripline monopulse comparator with two segments. Our novel design applies the stripline in the back-end which considerably reduces the antenna's backward radiation. The shaped patterns in the E and H planes are achieved by tapering patch widths and adjusting the impedance transformer of each subarray. Four half power quadrature hybrids are combined to form 2D monopulse feeding in the back-end. Both parts adopt a simple symmetrical layout that simplifies the design process. The measured reflection coefficients of each port are lower than −10 dB across 34.5 GHz to 35.5 GHz working band meanwhile isolation between these ports are better than 25 dB. Furthermore, the first side lobe level (FSLL) in the sum beam, which is remarkably suppressed by Taylor synthesis design method, achieves about −24 dB both in E and H planes. The measured gain of the sum pattern achieves 25.3 dBi at 35 GHz center frequency, while the nulling depth of the difference patterns in both planes are lower than −30 dB.

INDEX TERMS Series-fed planar microstrip array antenna, two dimensional monopulse tracking, Ka-band compact radar, stripline comparator network.

I. INTRODUCTION

The millimeter wave (MMW) band has many intrinsic advantages in developing small-scale or portable radar equipment. Miniature MMW radar works flexibly and can be arranged easily. Therefore, there has been great interest in commercial automobile driver-assistance applications [1], [2]. However, due to the high operating frequency, MMW radar is generally constrained to functioning in some relatively short-range applications [3]. The Ka-band MMW has been widely applied in airborne and air defense radar systems for its acceptable transmission link loss [4]–[6]. In addition, array antenna structures based on printed circuit boards (PCB) have the special characteristics of a low profile and light weight, which makes them more suitable in MMW scenarios than earlier metal designs such as four quadrant horn arrays with reflectors, and waveguide slot arrays [7], [8]. There have been many research studies about microstrip arrays with parallel or series feed technique [9]–[13], plate slots array [14] and substrate integrated waveguide (SIW) slots array [15]–[17]. There has been special interest in the microstrip array, which is less difficult to fabricate compared with SIW structures, and it is easier to synthesize the desired pattern through various designs of the element and feed networks [18]–[24]. In [19], six series-fed microstrip linear subarrays with tapered patch width distribution and a single-end connecting SIW parallel feed network were used to form shaped patterns in azimuth and elevation cut planes. In [20], a series of patches with tapered width and impedance transformers were utilized to form a planar microstrip array for automobile radar long range detection. An ideal first side lobe level (FSLL) of approximately −20 dB was achieved in its E and H planes.

The associate editor coordinating the review of this manuscript and approving it for publication was Chinmoy Saha.

A 6-port 3 × 3 and a 4-port 2 × 2 series-fed planar array were introduced in [21] and [22], respectively. Both designs adopted excitations from two orthogonal directions to provide dual-polarized characteristics and hence were ideally qualified for X-band airborne synthetic aperture radar (SAR) applications. A K-band linear array consisting of ten series-fed rectangular patches was proposed in [23], where the Chebyshev excitation distribution was realized by adjusting each patch's width. For the joint requirements of dual band, dual polarization, compact structure and low cost, the antennas shown in [21] and [23] were further integrated into a shared aperture antenna (SAA) in [24].

This study further develops the planar series-fed array layout used in [20] to the Ka-band monopulse array antenna design. To suppress the FSLL in sum patterns, the Taylor synthesis method is used in the first quadrant planar array design, which is then mirror symmetrically arranged about x-axial and y-axial to obtain the four-quadrant front-end. We noted that four ring couplers in [9], [10] and four quadrature hybrids in [11]–[15] can be combined to form a two-dimensional (2D) monopulse comparator network. Drawing lessons from these ideas, our study uses four 3 dB two-branch-line couplers to generate sum and difference patterns simultaneously, similar to [25]. Moreover, an alternative scheme of stripline feeding is introduced in this work, where the upper and lower stripline layer connect front-end and bottom coaxial feed probe via metallized blind holes respectively. This improves the undesired back lobe caused when a microstrip feed line is exposed to the bottom side of substrate as in [12]–[14], as well as the high processing cost of the SIW-based back-end as in [15]. In our design, both the radiation array and back-end network have a symmetrical layout and are separated by the stripline upper ground. The compact stripline feeding layout in our design has the four series feed planar arrays located at four quadrants in xoy plane that are fed through four metallized vias close to the center of board. This realizes the specific excitation distributions with a maximum amplitude at the center of the four-quadrant array. Therefore, optimized radiation characteristics can be easily achieved with this compact stripline comparator structure. Low FSLL sum patterns are produced in the forward radiation while the backward radiation is greatly suppressed. The whole antenna structure and design flow are greatly simplified by our design. The design's ideal FSLL, front to back ratio (FBR), and null depth in its E/H plane sum and difference patterns are obtained across 34.5 GHz to 35.5 GHz working band. This design performance was verified by highly consistent simulated and measured results.

This paper is organized as follows: the theoretical synthesis based on radiation pattern solutions and resulting four-quadrant array configuration are given in Section II. Based on this layout, the simulation designs of radiation array front-end and monopulse comparator back-end are successively shown in Section III. Section IV gives the fabricated antenna model and its measured performance, which are then compared with the simulated ones. Finally, the conclusion is in section V.

II. ARRAY TOPOLOGY AND THEORETICAL DESIGN

A. THEORETICAL ANALYSIS

The arrangement of the designed front-end array with the substrate center as the coordinate origin is shown in Fig. 1. Each quadrant comprises M × N rectangular patches and symmetrically locates them at the xoy plane with respect to the x and y axis. It is convenient for the analytic derivation to take the first quadrant as the reference to obtain the patterns of the entire front-end.

Each quadrant array is composed as follows. N patches with the same length and tapered width distribution are series-fed and uniformly arranged along the y-axis to form M subarrays. The M subarrays are then connected by M − 1 sections of main feed line and an impedance transformer along the x-axis to form the uniform planar array. Taking the element closest to origin point as initial values of m=1, n=1, then each element position coordinate can be expressed as (x_m, y_n). The lower side is taken as the reference position of each patch's edge voltage. For purpose of convenience, here the patch edge voltage in each subarray is approximately treated as invariable. Under this approximation, the width and edge voltage phasor of each patch element can be denoted as W_n and U_m, respectively.

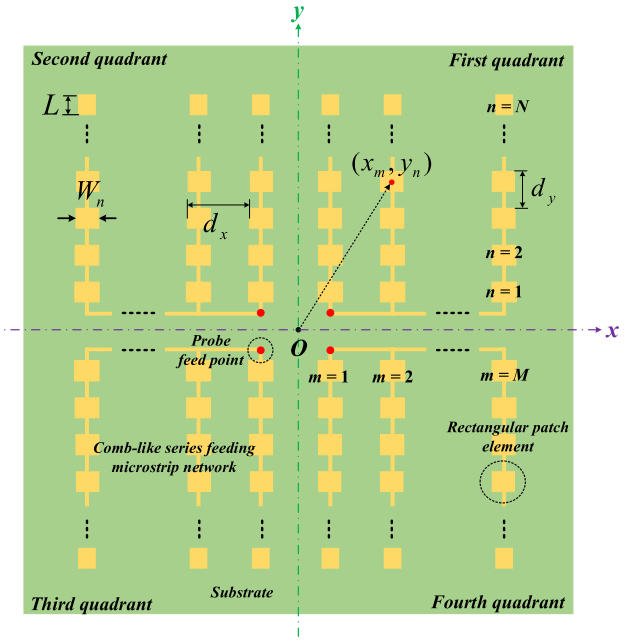

FIGURE 1. Four-quadrant microstrip array front-end with symmetric arrangement in xoz plane.

The equivalent magnetic current of each element flows in x direction which determines the y and z direction components of electric field as the main-polarization, and the x component as the cross-polarization. Thus, the two cut planes can be defined as E plane (yoz) and H plane (xoz). Taking the probe to the ground as the reference direction of excitation voltage at each quadrant's feed point, then each feed voltage phasor can be written as U_I, U_{II}, U_{III} and U_{IV}. In the ideal

case, the four voltages need to be at a constant-amplitude. According to the phase relationship between them, the patterns of entire four quadrant array can be composed as follows:

1) SUM PATTERNS IN E AND H PLANES

The U_I, U_{II} have same phase and U_{III}, U_{IV} have same phase but these two pairs are out of phase. This can be expressed as $U_I = U_{II} = -U_{III} = -U_{IV}$. Under the infinite ground case, the antenna radiates sum patterns in both E and H planes simultaneously. The patterns' formulas can be derived by superposition principle are given as:

$$f_{E\cdot\sum}(\theta) = \left|\cos(\frac{1}{2}k \cdot L \cdot \sin\theta) \cdot \sum_{n=1}^{N} W_n \cdot \cos(k \cdot y_n \cdot \sin\theta)\right| \tag{1}$$

$$f_{H\cdot\sum}(\theta) = \left|\cos\theta \cdot [\sum_{n=1}^{N} W_n \cdot Sinc(\frac{1}{2}k \cdot W_n \cdot \sin\theta)] \cdot [\sum_{m=1}^{M} U_m \cdot \cos(k \cdot x_m \cdot \sin\theta)]\right| \tag{2}$$

2) DIFFERENCE PATTERNS IN E PLANE

All of the four voltages have same phase, which is $U_I = U_{II} = U_{III} = U_{IV}$. Here the antenna generates difference patterns in its E plane, whose formula is:

$$f_{E\cdot\Delta}(\theta) = \left|\cos(\frac{1}{2}k \cdot L \cdot \sin\theta) \cdot \sum_{n=1}^{N} W_n \cdot \sin(k \cdot y_n \cdot \sin\theta)\right| \tag{3}$$

3) DIFFERENCE PATTERNS IN H PLANE

The U_I, U_{III} have same phase and U_{II}, U_{IV} have same phase but these two pairs are out of phase, namely $U_I = U_{III} = -U_{II} = -U_{IV}$. In this case, the antenna generates difference patterns in H plane:

$$f_{H\cdot\Delta}(\theta) = \left|\cos\theta \cdot [\sum_{n=1}^{N} W_n \cdot Sinc(\frac{1}{2}k \cdot W_n \cdot \sin\theta)] \cdot [\sum_{m=1}^{M} U_m \cdot \sin(k \cdot x_m \cdot \sin\theta)]\right| \tag{4}$$

where k is the wave number in free space.

B. TAYLOR SYNTHESIS

This antenna is designed for application as a ground-based monopulse radar for airspace detection purpose, where the abilities of anti-interference in the near ground clutter environments and distinguishing the false targets are strongly needed. Hence the antenna design requires that the pattern's feature that the SLL can gradually decrease with the angle deviates from the main lobe direction. For this reason, the Taylor synthesis method is adopted to suppress FSLL of sum patterns. First, the size of array plane and element number M, N should be determined by the composite demands of antenna gain and half power beam width (HPBW). From (1), for the linear patch array, the excitation amplitude coefficient of each element in the sum of N terms can be controlled by adjusting each patch's width W_n. Hence in the subsequent front-end design, the patch lengths L are designed to be constant while the patch widths W_n are modulated to control the amplitude distribution in each linear subarray. Then the E-plane sum pattern can be synthesized by (1). The N patch widths of each subarray are obtained by the help of MATLAB programming. According to the input target FSLL value and uniform linear array profiles including element's number and spacing, this software calls the classical Taylor synthesis algorithm to complete the FSLL optimization of (1) and outputs a N-dimensional array including each patch's normalized width scale factor. The resulting width distributions are then substituted into (3) to determine the H-plane sum pattern and excitation voltage U_m of each subarray. In the following front-end design discussion, it will be explained how this excitation voltage distribution is realized by adjusting the quarter wavelength impedance transformers related to each subarray. As mentioned above, given the symmetry of four quadrant array layout, all of the analyses are referred to the first quadrant parameters.

The element number in our design are set to M=8, N=10. Target values of FSLL are expected to be −30 dB in both E and H plane pattern synthesis. The resulting normalized excitation amplitudes are listed in Table 1. The theoretical synthesis results of the radiation patterns are shown in Fig. 3, about 6° of HPBW is achieved in the two cut planes. Since the $\cos\theta$ factor is included in H plane patterns as exhibited in (2) and (4), the amplitude in H plane decays more rapidly along with the deviation increasing from the 0° direction compared with the E plane and obtains null at the end-fire direction.

III. ANTENNA SIMULATION DESIGN

A. FOUR-QUADRANT FRONT-END

As mentioned in II. B, the first step in front-end design is to optimize the linear patch array with tapered width distributions for obtaining desirable E plane sum patterns. Hence the design of the center patch element numbered n=1 is first conducted to determine its width W_1 and length L_1, then other patches' width W_2-W_{10} are set according to the normalized Taylor weighted coefficients shown in Table 1. In these design steps of the single element, the initial size is calculated based on the ordinary formulas introduced in [26], and then a simulated model is established and optimized by ANSYS HFSS software. Fig. 2 shows the simulated single patch and its optimized radiation patterns. At 35 GHz center frequency, the simulated directivity and gain reach 8.4 dBi and 7 dBi providing about 70% radiation efficiency. Based on the given HPBW in E and H planes, the directivity of four quadrant array's sum patterns can be estimated as

TABLE 1. Normalized excitation amplitudes of single quadrant elements obtained by Taylor synthesis method.

1-D linear subarray		2-D planar array	
Patch's number	Normalized amplitude	Subarray's number	Normalized amplitude
n = 1	1	m = 1	1
n = 2	0.9648	m = 2	0.9444
n = 3	0.899	m = 3	0.8433
n = 4	0.8082	m = 4	0.7069
n = 5	0.6971	m = 5	0.5492
n = 6	0.573	m = 6	0.3981
n = 7	0.4494	m = 7	0.29
n = 8	0.3445	m = 8	0.2512
n = 9	0.2748		
n = 10	0.2505		

follows [27]:

$$D_{array} = \frac{4\pi}{\Delta\theta_E \cdot \Delta\theta_H} \tag{5}$$

where $\Delta\theta_E$ and $\Delta\theta_H$ in radians are HPBW of E and H plane patterns, respectively. As mentioned in Section II. B that about 6° of HPBW is achieved in E and H plane theoretical synthesis patterns. According to these theoretical values, about 30 dBi is estimated as the four-quadrant array's directivity. While for the array gain, the radiation efficiency η_r of front-end should be considered:.

$$G_{array} = \eta_r \cdot D_{array} \tag{6}$$

In view of the simulated efficiency in a single element, a larger-scale radiation array will cause more power losses, here the radiation efficiency is roughly taken as 60% as an approximate estimation, that is, the power loss caused by array conductor losses and dielectric losses is about 2 dB. Empirically, for practical applications, this approximate estimation can achieve accuracy with better than 10% absolute value. So the front-end array gain is preliminarily estimated to be 28 dBi.

A simulated model of the front-end array shown in Fig. 4 was also established by ANSYS HFSS based on: the array configuration, the distribution of the patch width, and the subarray excitation voltage obtained in section II. Each quadrant array comprises eight linear subarrays which includes ten tapered width patches. This comb-like planar array is fed

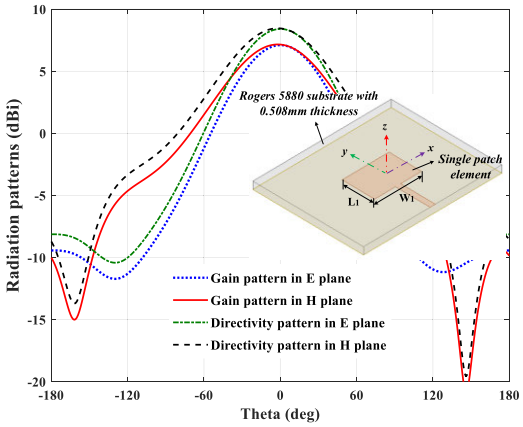

FIGURE 2. Simulated single patch element and its optimized radiation patterns at 35 GHz center frequency.

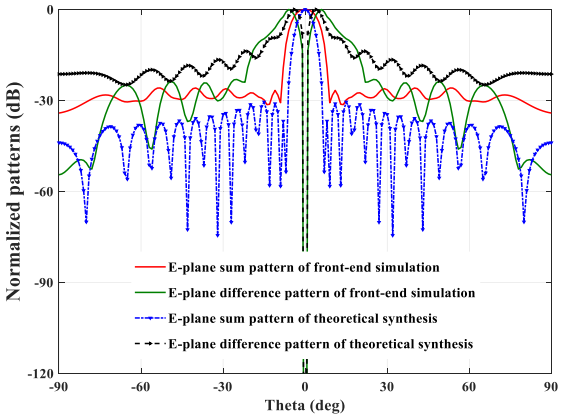

(a)

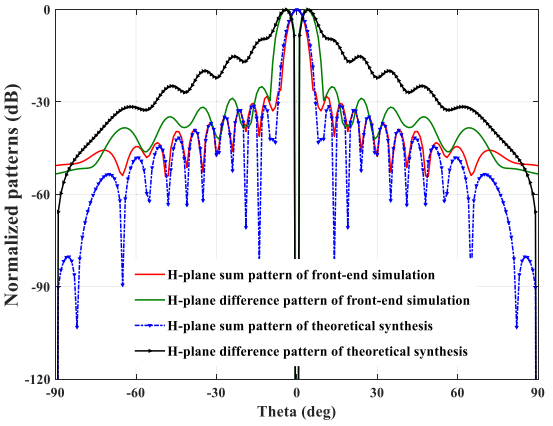

(b)

FIGURE 3. Theoretical synthesis and HFSS-based simulated patterns of four-quadrant microstrip array: (a) E plane patterns at 35 GHz center frequency, (b) H plane patterns at 35GHz center frequency.

at the point closest to the origin by an inserted probe with 0.4 mm diameter, which can be replaced by metallized blind hole in actual processing.

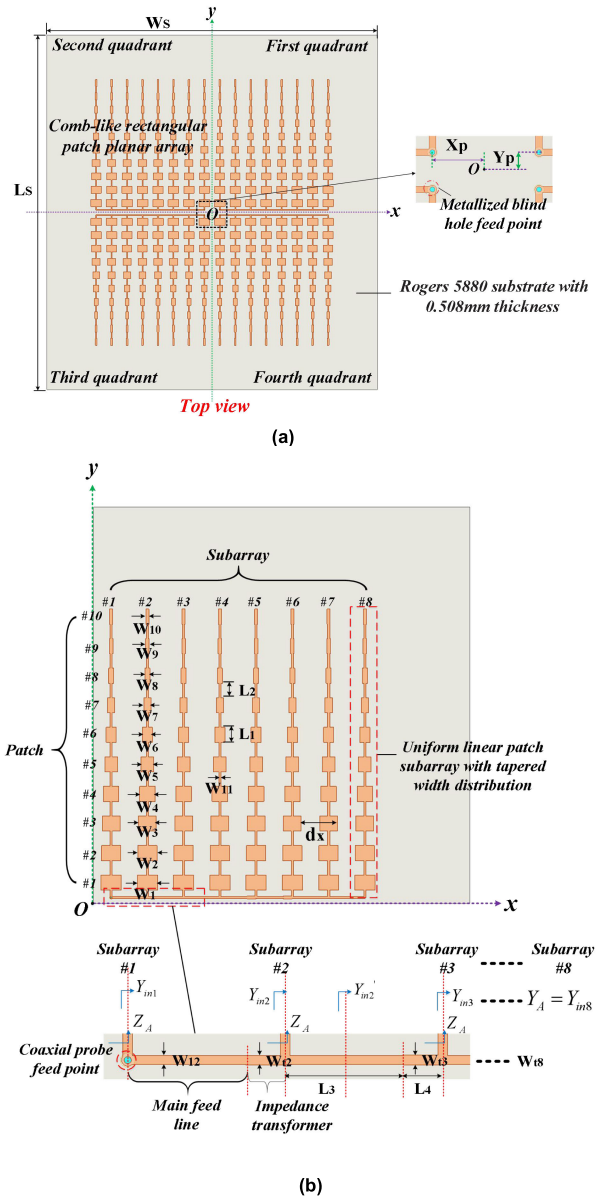

FIGURE 4. Simulation model of four-quadrant microstrip array front-end: (a) whole four-quadrant array structure, (b) planar array in each quadrant and its significance of equivalent circuit parameters.

The patch width distribution is made to be consistent with Taylor synthesis result to form the weighted excitation required for E plane, while a few impedance transformer sections are used to shape H plane patterns. The optimized parameters are listed in Table 2. The simulated patterns are shown in Fig. 3 for comparison with the theoretical counterparts. The simulated sum pattern in H plane and difference patterns correspond well with the theoretical prediction.

However, the E plane sum pattern deteriorates to a certain extent. The HPBW is wider about 4° than the theoretical value, and the sidelobe has an obvious upward trend along with the deviation angle increasing. One of the main reasons

TABLE 2. Optimized parameters of designed front-end segment.

Parameter	Value (mm)	Parameter	Value (mm)	Parameter	Value (mm)
L_1	2.82	W_7	1.582	W_{t6}	0.466
L_2	2.64	W_8	1.098	W_{t7}	0.394
L_3	4.74	W_9	0.779	W_{t8}	0.37
L_4	1.58	W_{10}	0.667	Ls	145
W_1	4.35	W_{11}	0.4	Ws	135
W_2	4.174	W_{12}	0.381	Yp	1.1
W_3	3.833	W_{t2}	0.403	Xp	3.16
W_4	3.355	W_{t3}	0.418	dx	6.32
W_5	2.78	W_{t4}	0.442		
W_6	2.167	W_{t5}	0.478		

for this phenomenon is mutual coupling between each subarray. In addition, due to the incomplete guided wave energy radiation along the x axis, the electric field near the edge of the subarray is much stronger than expected in the ideal Taylor weighted result. Nevertheless, the simulation FSLL is lower than −28 dB, which is acceptable for the system requirements. It is worth noting that the excitation source is set up as a coaxial port at the bottom microstrip ground in the simulation model. This port as interface between front-end and back-end can be included in conducted impedance matching calculation by using the equivalent circuit of each quadrant array shown in Fig. 5. It should be pointed out that each linear subarray is only treated as a equivalent shunt admittance in this model. While for the main microstrip transmission line, it is not refined into the classical CLR model where lots of infinitesimal lumped-element circuits work as basic cascade units. According to the transmission line analysis method, the input impedance at ground coaxial port can be deduced as shown in (7). In this comb-line structure, the normalized excitation coefficient of each subarray can be obtained by shunt principle of parallel circuit, as shown in (8).

$$Z_{in1} = \frac{Z_A}{1 + k_2^2 + (k_2 \cdot k_3)^2 + \cdots\cdots + \prod_{m=2}^{M} k_m^2} \tag{7}$$

$$I_m = \prod_{i=2}^{M} k_i^2 \cdot I_1, \quad m = 2, 3 \cdots\cdots, M \tag{8}$$

$$k_m = Z_{cm}/Z_c, \quad m = 2, 3 \cdots\cdots, M \tag{9}$$

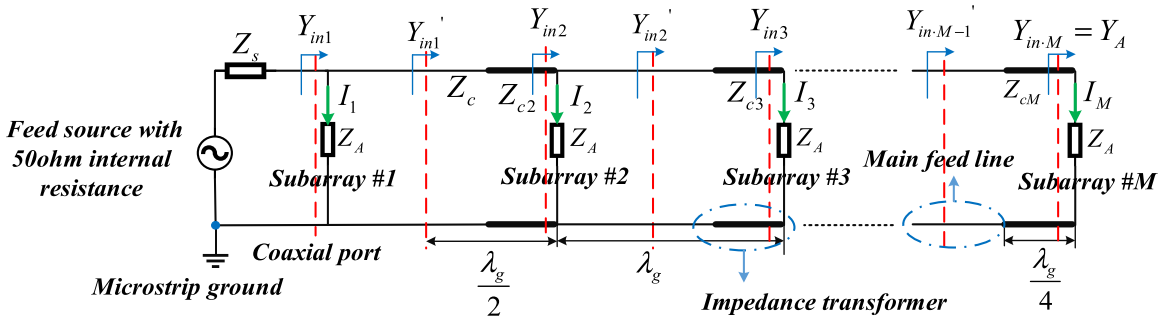

FIGURE 5. Transmission line equivalent circuit model of each quadrant planar array shown in Fig. 4 (b).

All of the parameters should be adjusted to make the subarray excitation I_m distribute according to the specific rules derived by Taylor method. As to our design, the first step is calculating characteristic impedance of each transformer section by (8) and (9) according to the weighted proportional distribution obtained from the previous section. The characteristic impedance Z_c of the main feed line is set to 100 ohms here, and then each transformer's impedance Z_{cm} can be calculated.

Finally, the required subarray's input impedance Z_A is obtained by (7). Fortunately, due to the stripline structure adopted in back-end, the radiation layer and feed layer are separated by the ground. As long as the excitation signals at the four ports meet the specific amplitude and phase relationship mentioned in section II. A, the antenna can generate the ideal patterns. It should be pointed out that to realize the impedance matching between the two segments, identical port impedance of four quadrants' interface need to be considered in the independent front-end and back-end simulation procedure. The next section will introduce how to achieve such specific excitation performances through the back-end design.

B. MONOPULSE COMPARATOR BACK-END

As discussed above, in order to generate desired patterns in E and H planes, the voltages at four interfaces should be in accordance with specific amplitude and phase relationship introduced in section II. A. In view of some published works on planar monopulse comparators such as [13], [14], combining the four directional couplers to form a 2D comparator is a convenient solution. Consequently, it is used in this design. Moreover, an improved substitution of the stripline back-end is introduced in our model. This can prevent the microstrip feeders exposed to the PCB bottom side from causing a large back lobe and seriously deteriorating the patterns' front-to-back ratio (FBR) [14]. This improved substitution of the stripline back-end can improve the complicated air gap structure adopted in [13], which can obviously reduce backward radiation and keep the antenna's low profile and easy processing.

The functional block diagram of the 2D monopulse comparator is presented in Fig. 6. Four 3 dB quadrature

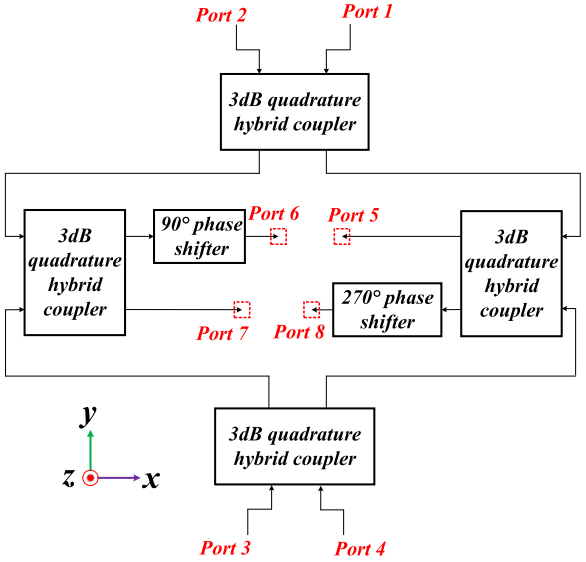

FIGURE 6. Functional block diagram of 2D monopulse comparator.

hybrid couplers are located in the upper, lower, left and right positions of stripline middle layer conductor. Ideally, two-channels of coupler output signals which have equal amplitude and phase quadrature can be achieved when the excitation is only fed into one of the four input ports numbered 1 to 4. This feature is utilized to make the port 5 to port 8 which connect four quadrant arrays to generate the required output relationships. When working as a transmitting antenna, the 8-port back-end's port 1-port 4 are input ports and port 5-port 8 are output ports. The transmission coefficients from four input ports to four output ports and resulted pattern under four input conditions are derived as follows for the design structure proposed in Fig. 8, according to the S-parameters of two-branch-line coupler introduced in [25] and without regard to the transmission attenuation and delay except for the four two-branch-line couplers and two phase shifters.

1) INPUT FROM PORT 1

When the signal is input from port 1, the transmission coefficients from port 1 to port 5-port 8 are derived

in equation (10).

$$\begin{cases} S_{5\cdot1} = (\frac{1}{\sqrt{2}} \cdot \angle -90°) \cdot (\frac{1}{\sqrt{2}} \cdot \angle -90°) = -\frac{1}{2} \\ S_{6\cdot1} = (\frac{1}{\sqrt{2}} \cdot \angle -180°) \cdot (\frac{1}{\sqrt{2}} \cdot \angle -90°) \\ \quad \cdot(\angle -90°) = \frac{1}{2} \\ S_{7\cdot1} = (\frac{1}{\sqrt{2}} \cdot \angle -180°) \cdot (\frac{1}{\sqrt{2}} \cdot \angle -180°) = \frac{1}{2} \\ S_{8\cdot1} = (\frac{1}{\sqrt{2}} \cdot \angle -90°) \cdot (\frac{1}{\sqrt{2}} \cdot \angle -180°) \\ \quad \cdot(\angle -270°) = -\frac{1}{2} \end{cases} \tag{10}$$

From (10) it can be observed that in the port 1 input situation, port 5 and port 8 outputs are in phase, and port 6 and port 7 outputs are in phase, while the two pairs of signals are opposition. Simulated result of corresponding surface current vectors distribution on four-quadrant patches array and its diagrammatic sketch of equivalent magnetic currents are shown in Fig. 7 (a), from which it can be concluded that the radiation in both E and H planes are canceled out. So, port 1 is normally unused and connects to a 50 ohm matched load.

2) INPUT FROM PORT 2

When the signal is input from port 2, the transmission coefficients from port 2 to port 5-port 8 are derived in equation (11).

$$\begin{cases} S_{5\cdot2} = (\frac{1}{\sqrt{2}} \cdot \angle -180°) \cdot (\frac{1}{\sqrt{2}} \cdot \angle -90°) = \frac{j}{2} \\ S_{6\cdot2} = (\frac{1}{\sqrt{2}} \cdot \angle -90°) \cdot (\frac{1}{\sqrt{2}} \cdot \angle -90°) \\ \quad \cdot(\angle -90°) = \frac{j}{2} \\ S_{7\cdot2} = (\frac{1}{\sqrt{2}} \cdot \angle -90°) \cdot (\frac{1}{\sqrt{2}} \cdot \angle -180°) = \frac{j}{2} \\ S_{8\cdot2} = (\frac{1}{\sqrt{2}} \cdot \angle -180°) \cdot (\frac{1}{\sqrt{2}} \cdot \angle -180°) \\ \quad \cdot(\angle -270°) = \frac{j}{2} \end{cases} \tag{11}$$

From (11) can be observed that, in the port 2 input situation, all of the four output signals are in phase. Simulated results of the corresponding surface current vectors distribution on four-quadrant patches array and its diagrammatic sketch of equivalent magnetic currents are shown in Fig. 7 (b). Each quadrant's feed point, which is port 5 and port 8, are located at the edge corner closest to the coordinate origin, and the four ports are symmetrically distributed about x-axis and y-axis. Therefore, the surface currents at the upper and lower patches symmetrically distributed about x-axis will flow reversely. In this case, the radiation in H plane is canceled out, while in E plane it can form a difference pattern with nulling at +z direction. So, port 2 is used as E plane difference port in the proposed design.

3) INPUT FROM PORT 3

When the signal is input from port 3, the transmission coefficients from port 3 to port 5-port 8 are derived in equation (12).

$$\begin{cases} S_{5\cdot3} = (\frac{1}{\sqrt{2}} \cdot \angle -180°) \cdot (\frac{1}{\sqrt{2}} \cdot \angle -180°) = \frac{1}{2} \\ S_{6\cdot3} = (\frac{1}{\sqrt{2}} \cdot \angle -90°) \cdot (\frac{1}{\sqrt{2}} \cdot \angle -180°) \\ \quad \cdot(\angle -90°) = \frac{1}{2} \\ S_{7\cdot3} = (\frac{1}{\sqrt{2}} \cdot \angle -90°) \cdot (\frac{1}{\sqrt{2}} \cdot \angle -90°) = -\frac{1}{2} \\ S_{8\cdot3} = (\frac{1}{\sqrt{2}} \cdot \angle -180°) \cdot (\frac{1}{\sqrt{2}} \cdot \angle -90°) \\ \quad \cdot(\angle -270°) = -\frac{1}{2} \end{cases} \tag{12}$$

From (12) it can be observed that in the port 3 input situation, port 5 and port 6 outputs are in phase, and port 7 and port 8 outputs are in phase, while the two pairs of signals are opposition. Simulated results of the corresponding surface current vectors distribution on four-quadrant patches array and its diagrammatic sketch of equivalent magnetic currents are shown in Fig. 7 (c). In this case, the surface currents in four quadrants flow in same direction. Therefore, their radiations in both E and H planes can be superimposed in phase and simultaneously form sum patterns in the two orthogonal cut planes. So, port 3 is used as the E and H planes sum port in this design.

4) INPUT FROM PORT 4

When the signal is input from port 4, the transmission coefficients from port 4 to port 5-port 8 are derived in equation (13).

$$\begin{cases} S_{5\cdot4} = (\frac{1}{\sqrt{2}} \cdot \angle -90°) \cdot (\frac{1}{\sqrt{2}} \cdot \angle -180°) = \frac{j}{2} \\ S_{6\cdot4} = (\frac{1}{\sqrt{2}} \cdot \angle -180°) \cdot (\frac{1}{\sqrt{2}} \cdot \angle -180°) \\ \quad \cdot(\angle -90°) = -\frac{j}{2} \\ S_{7\cdot4} = (\frac{1}{\sqrt{2}} \cdot \angle -180°) \cdot (\frac{1}{\sqrt{2}} \cdot \angle -90°) = \frac{j}{2} \\ S_{8\cdot4} = (\frac{1}{\sqrt{2}} \cdot \angle -90°) \cdot (\frac{1}{\sqrt{2}} \cdot \angle -90°) \\ \quad \cdot(\angle -270°) = -\frac{j}{2} \end{cases} \tag{13}$$

From (13) can be observed that, in the port 4 input situation, port 5 and port 7 outputs are in phase, and port 6 and port 8 outputs in phase, while the two pairs of signals are opposition. Simulated result of corresponding surface current vectors distribution on four-quadrant patches array and its diagrammatic sketch of equivalent magnetic currents are shown in Fig. 7 (d). In this case, the surface currents at the left and right patches symmetrically distributed about y-axis flow reversely, hence difference pattern in H plane will be radiated. So, the port 4 is used as H plane difference port in our design.

The designed stripline comparator network based on Fig. 6 is shown in Fig. 8. In the model, four coaxial converters

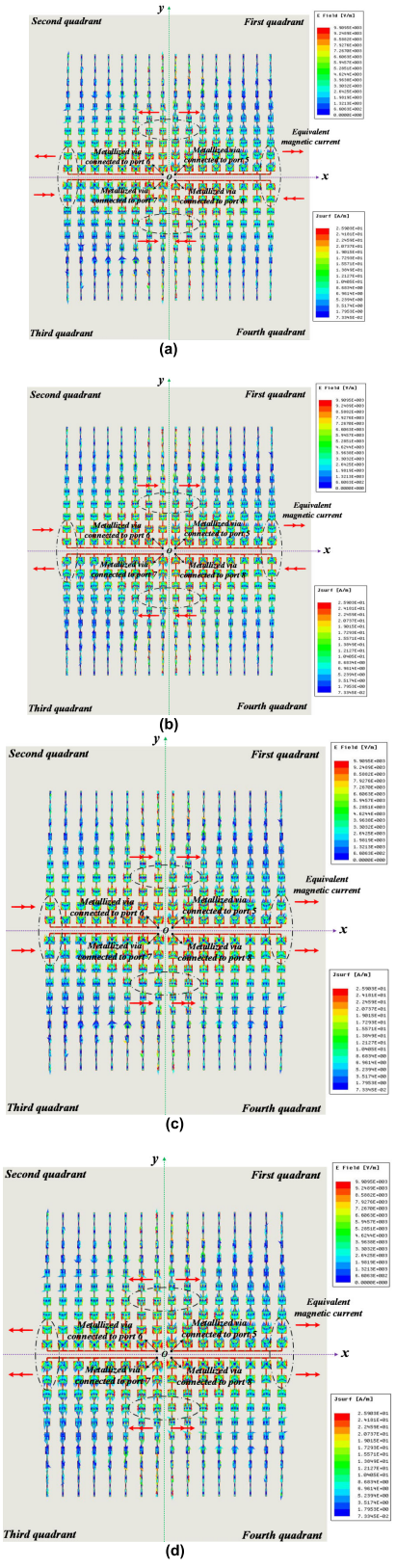

FIGURE 7. Simulated surface current vector and electric intensity distributions on four-quadrant patches array under four back-end's input conditions: (a) input from port 1, (b) input from port 2, (c) input from port 3, (d) input from port 4.

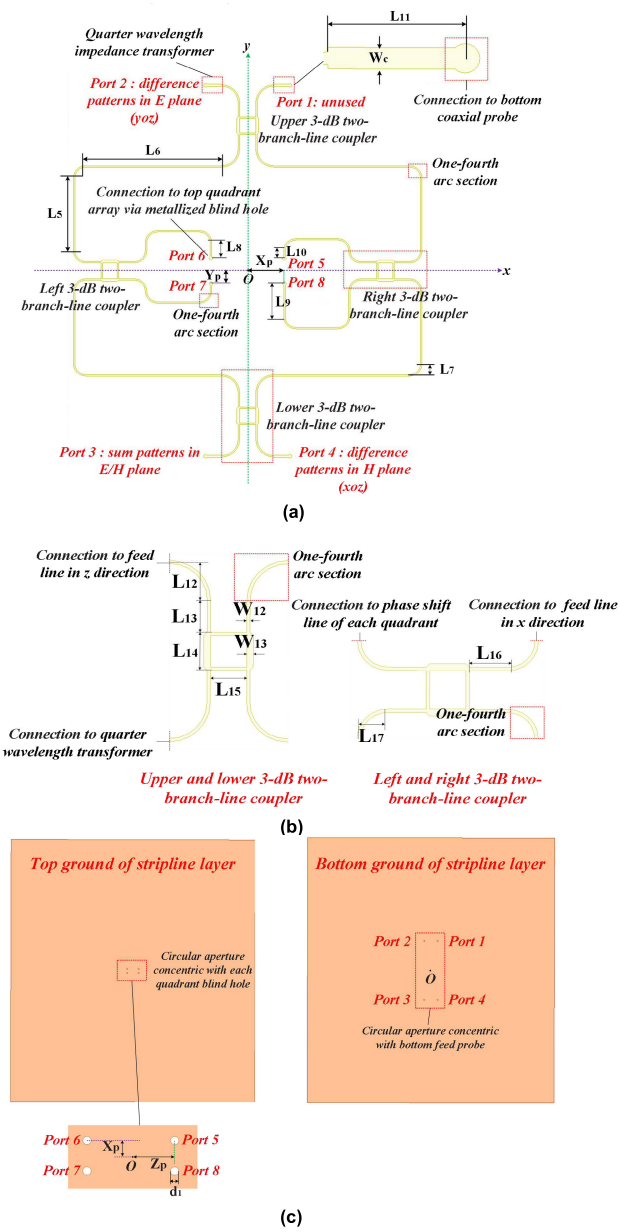

FIGURE 8. Simulation model of 2D monopulse comparator stripline network: (a) feed line writing of middle conductor, (b) structure of four 3dB quadrature hybrids used in Fig. 6 (a), (c) top and bottom ground.

with 0.3 mm diameter probe are inserted into port 1 to port 4 for transferring to a coaxial cable or matching load component. The port 5 to port 8 are connected to front-end arrays in four quadrant planes via metallized blind holes with 0.4 mm diameter penetrate the top microstrip board and stripline upper layer. The whole feeding layer is structured on a Rogers-5880 substrate with 0.508 mm thickness. The two phase shifters connecting port 6 and port 8 in Fig. 6 are realized by two feed line sections with 0.25 and 0.75 electrical lengths, respectively. Each parameter is tuned to make the comparator meet required performance, which is equivalent to optimizing the S-parameters of this eight-port network.

TABLE 3. Optimized parameters of designed back-end segment.

Parameter	Value (mm)	Parameter	Value (mm)	Parameter	Value (mm)
L_5	6.343	L_{11}	1.39	L_{17}	1
L_6	11.693	L_{12}	1.5	W_{12}	0.124
L_7	1	L_{13}	1.4	W_{13}	0.25
L_8	1.352	L_{14}	1.39	W_c	0.22
L_9	2.897	L_{15}	1.39	d_1	0.6
L_{10}	0.657	L_{16}	1.4		

The optimization dimensions are listed in Table 3. The simulated transmission coefficients from three functional input ports to four output ports are revealed in Fig. 9 and Fig. 10, from which it can be seen that all groups of transmission coefficients approximately meet the required amplitude and phase relationship across the working band and approach perfect features near the 35 GHz center frequency.

As the frequency deviates from center point, the transmission attenuation corresponding each input fluctuates to some extent. The maximum imbalance between each curve is within 2 dB observed in the three amplitude panels and the phase deviations in each phase curves panel are less than 10°, which would cause patterns' asymmetry nearby edge frequencies. The main reason for this phenomenon is the narrow bandwidth of phase shifters realized by extending feed line. Also, due to the large dielectric losses in the MMW band, the maximum transmission loss reaches an inferior −10 dB in the designed back-end structure. In fact, the dielectric losses existing in the front and back-end pose the most important factor in the antenna realized gain degradation.

IV. ANTENNA FABRICATION AND MEASUREMENT

A. INTEGRATED MODEL AND PHYSICAL PROCESSING

The simulated model of whole antenna structure is shown in Fig. 11 (a). The front-end and back-end are combined into a multilayer PCB board while a duralumin back-up with 5.5 mm thickness is added at back of the board to ensure the array's flatness for tooling requirements. For actual processing, two TACONIC FR-27 bonding films with 0.1 mm thickness are added at the stripline top ground and middle feed line, respectively. Photographs of the fabricated antenna board achieved by multilayer PCB technology and the dorsal duralumin back-up are exhibited in Fig. 11 (b) and (c), respectively. For the basic requirements of flatness, conductivity and oxidation resistance, a gold plating procedure was further conducted after the ordinary copper bonding in the whole PCB fabrication. A series of nylon screws with 2.2 mm diameter are used to tightly press the two parts together by penetrating the screw holes at edges. Four feed probes with 0.3 mm diameter are respectively inserted into port 1 to port 4 marked in Fig. 11 (b) to realize the excitation of whole antenna structure.

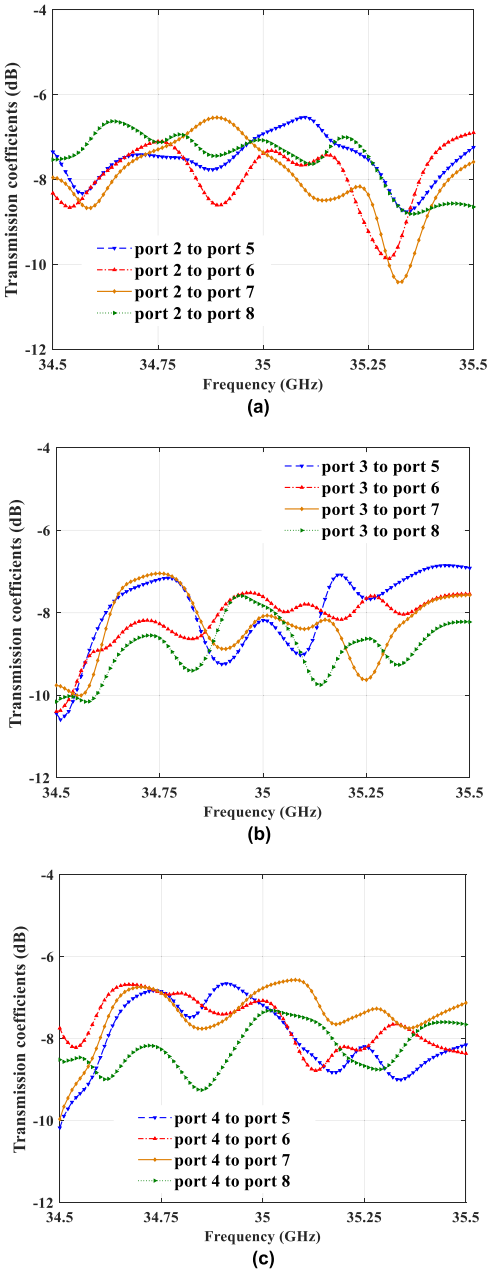

FIGURE 9. Simulated transmission coefficients' amplitudes from three functional input ports of port 2, port 3 and port 4 to four output ports corresponding to (a), (b) and (c), respectively.

It should be noted that due to the small spacing between port 1 and port 2 and between port 3 and port 4, the bottom side of duralumin back-up has no accommodation for a SMA coaxial connector with typical external diameter features. Therefore, four specially customized low loss RF cables with 0.5 m length are adopted in the overall fabricated model shown in Fig. 11 (d). One end of the cable connecting the hard aluminum plate is an SMP connector with only 3.7 mm external diameter, and the other end is a standard 2.92 mm coaxial connector. Four SMP probe connectors are fixed at the duralumin plate by a precise machining process. In the

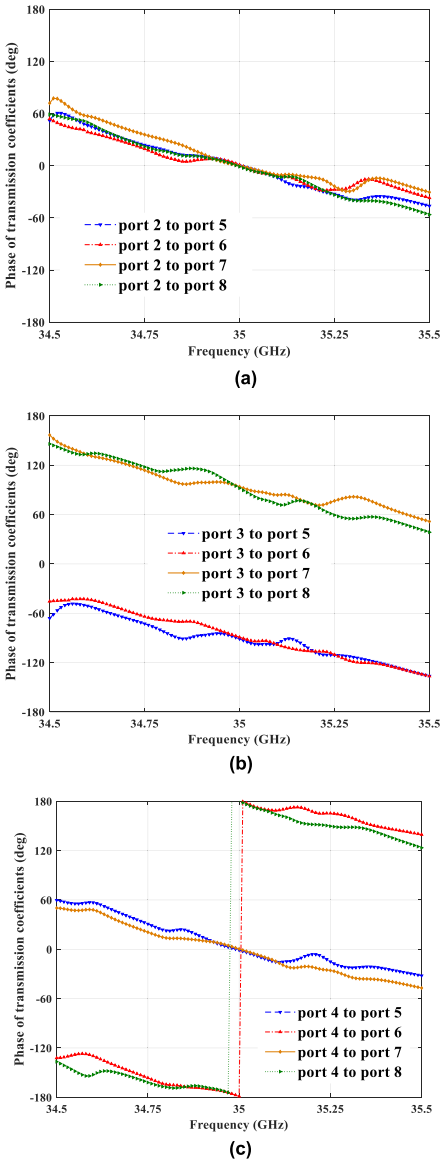

FIGURE 10. Simulated transmission coefficients' phases from three functional input ports of port 2, port 3 and port 4 to four output ports corresponding to (a), (b) and (c), respectively.

antenna test, the idle ports can connect 2.92 mm matched loads to minimize the interaction of the four ports.

Before the multilayer PCB processing, the antenna consists of three separated single-layer microstrip boards. The upper board is the microstrip front-end with 0.508 mm thickness. There are four penetrated metallized vias connected to the four quadrants' top array as shown in Fig. 4 (a). These four vias also need to be connected with port 5 and port 8 shown in Fig. 8 (a). The middle board is the upper stripline feeding layer shown in Fig. 12 (a). It also has four metallized vias concentric with ports 5 and port8 for connecting with the bottom middle feed line. The lower board is the lower stripline feeding layer shown in Fig. 12 (b). Its top side is mirror symmetric with middle board's bottom side. Its port 1–port 4 at the bottom ground are also connected with the top feed line by four metallized vias.

For the multilayer PCB processing, the first step is to press the upper and middle boards together by a 0.1 mm thickness solidified sheet. After this pressing, four metallized vias should be re-shaped at four quadrants array's feed points to penetrate the double-layered board. The second step is to press together the composite plate described above and the lower board by using the same type of solidified sheet. Before conducting the secondary pressing, the rectangular glue layer centered at the board with 30 mm $\times$ 35 mm area shown in Fig. 12 (b) should be scraped off for ensuring good contact between the two copper layers of feeding stripline. After finishing the three-ply board pressing, gold plating was made on the surfaces of top array and bottom ground. Finally, sixteen screw holes were drilled at the multilayer board's edges.

B. MEASUREMENT RESULT AND DISCUSSION

1) S-PARAMETERS

S-parameters of the whole processed model shown in Fig. 11 (d) are measured by Agilent-N5246A PNA-X vector network analyzer (VNA) shown in Fig. 13 (a). Fig. 13 (b) and (c) respectively present the simulated and measured results of the reflection coefficients and transmission coefficients on antenna's three functional ports denoted as Port 2, Port 3, and Port 4. The reflection coefficient of each port is lower than -10 dB across 34.5 GHz to 35.5 GHz working band. Undesirably, as compared with the smooth simulated curves, the measured S- parameters show some serious fluctuations between -10 dB and -20 dB, which can be also observed in the transmission coefficients. The isolation improves as the frequency increases mainly due to the cables' higher transmission losses, while the simulated and measured isolation between the three ports is better than 30 dB and 25 dB, respectively.

Through tuning analysis, three main factors cause the large deviations between measured and simulated results are found. First, the SMP to 2.92 mm adapter cables and coaxial match loads are used in the test procedure, which is not included in simulated model. Second, the imperfectly trimmed probe would extrude the PCB board and cause its misalignment to the PCB's ground port. Third, the calibration results obtained by KEYSIGHT N4694A electronic calibration module with calibration standards similar in accuracy to TRL are unsatisfactory, while some improvements such as de-embedding corrections are not performed. These factors together cause the fluctuation and deterioration of the measured S-parameters.

It should be noted that all of the above simulated and measured results are obtained under the condition required in conventional definition of S-parameters, where each idle port is connected to a matched load. To further explain the influences on S-parameter under open and short conditions, S-parameters related to port 2 in port 4's open and short conditions are discussed as follows. Assuming the excitation

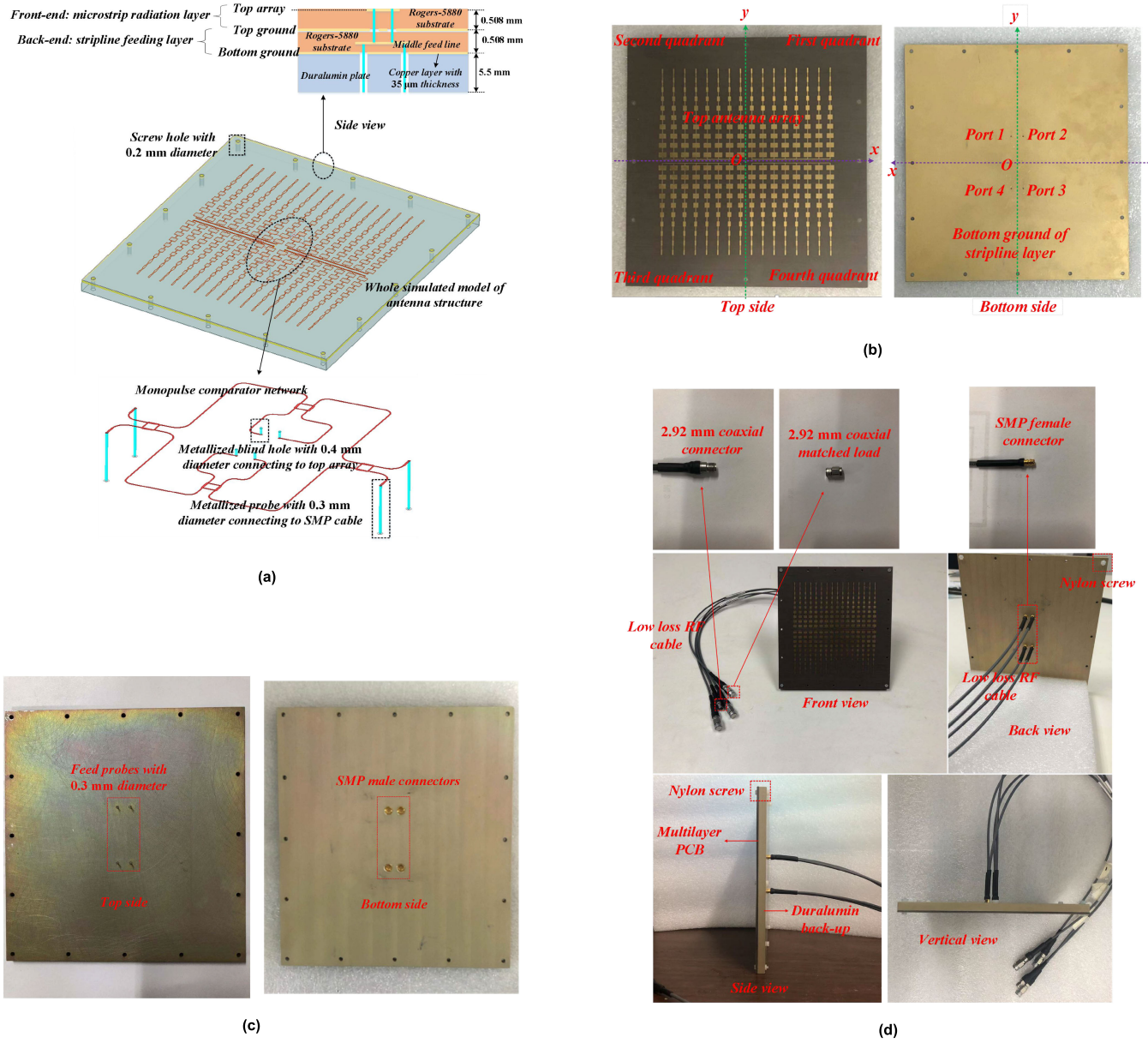

FIGURE 11. Simulated and fabricated models of whole antenna structure: (a) whole simulation model, (b) fabricated multilayer PCB composed of antenna's front-end and back-end, (c) fabricated duralumin back-up, (d) whole fabrication model.

is input from port 2, and port 4 is opened or shorted. In this case has been similarly discussed in [28], compared with the ideal load condition in S-parameter concepts, both outputs of port 2 and port 3 include two parts. One is that the signal reflects or transmits directly from port 2. The other is that the signal transmits from port 2 to port 4 first and then experiences total reflection at port 4's external opened or shorted terminal and secondarily transmits to port 2 or port 3. According to this analysis, the S-parameters related to port 2 in port 4's open and short conditions can be expressed as follows.

When port 4 is in an open condition, the voltage reflection coefficient at its external terminal is 1, the reflection coefficient of port 2 Γ_2 and the transmission coefficient from port 2 to port 3 T_{32} are shown in (14) and (15), respectively:

$$\Gamma_2 = S_{2\cdot2} + \frac{S_{4\cdot2}^2}{1 - S_{4\cdot4}} \tag{14}$$

$$T_{3\cdot2} = S_{3\cdot2} + \frac{S_{4\cdot2} \cdot S_{3\cdot4}}{1 - S_{4\cdot4}} \tag{15}$$

Similarly, the Γ_2 and T_{32} when port 4 is in short condition with -1 voltage reflection coefficient are shown in (16) and (17), respectively:

$$\Gamma_2 = S_{2\cdot2} - \frac{S_{4\cdot2}^2}{1 + S_{4\cdot4}} \tag{16}$$

$$T_{3\cdot2} = S_{3\cdot2} - \frac{S_{4\cdot2} \cdot S_{3\cdot4}}{1 + S_{4\cdot4}} \tag{17}$$

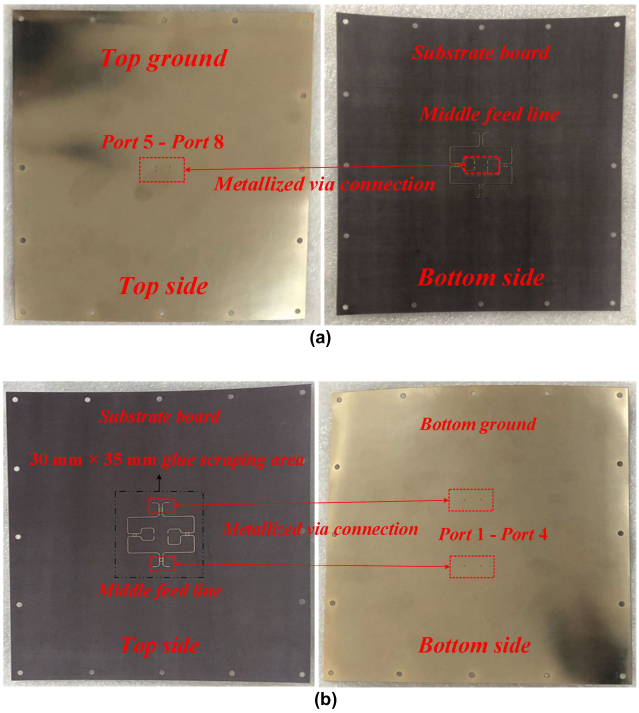

FIGURE 12. Fabricated models of stripline comparator photographed before multilayer PCB processing: (a) upper layer, (b) lower layer.

Since this design is an isotropic passive network, it has a symmetric S-matrix, which is utilized in (14) and (16). Comparisons between the theoretical S-parameter curves obtained by (14)-(17) with simulated curves are shown in Fig. 14. It can be seen that the deviations between theoretical and corresponding simulated results are rather small near the 35 GHz center frequency both in port 4's open and short conditions, which verifies our previous analysis.

2) RADIATION PATTERNS

The measured and simulated gain patterns at 35 GHz are revealed in Fig. 15. Both sum and difference patterns share good symmetries in E and H planes, which is mainly due to the symmetrical front-end array layout and ideal magnitude-phase characteristics of the back-end comparator. As to the sum patterns, measured gain reaches about 25.3 dBi, which is 3 dBi worse than simulated value. Compared with the front-end array introduced in III. A, the back-end's transmission loss should be considered in the whole antenna structure. Under the perfect impedance matching between front-end and back-end condition, the sum patterns' total gain of whole structure can be expressed as:

$$G_{total} = (|S_{53}|^2 + |S_{63}|^2 + |S_{73}|^2 + |S_{83}|^2) \cdot G_{array} \quad (18)$$

As to the back-end comparator, there are good consistencies appearing in the four transmission coefficients curves from the port 3 to port 5–port 8. All the amplitudes reach about −8 dB at 35 GHz center frequency against the −6 dB value in the ideal lossless back-end network.

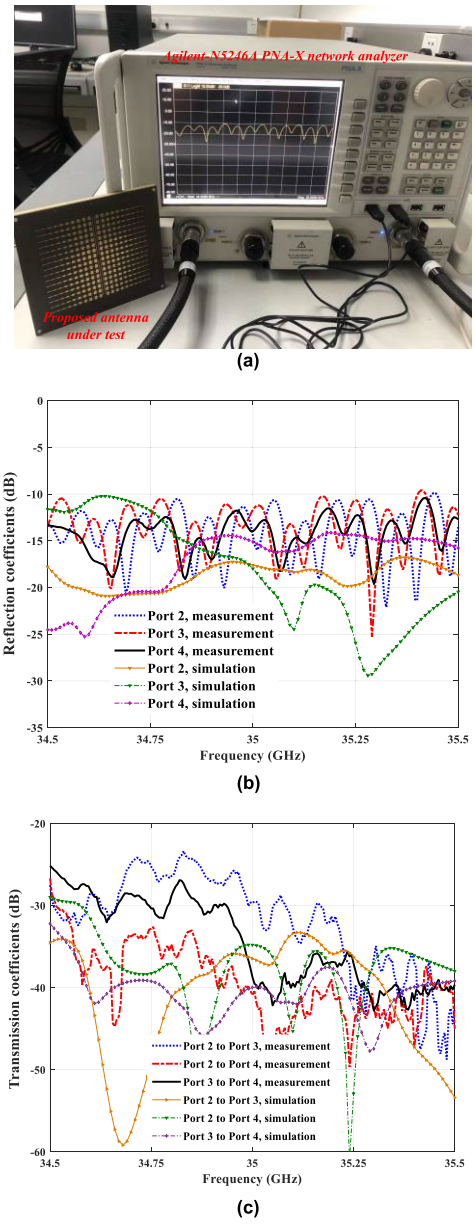

FIGURE 13. Simulated and measured S-parameters of antenna's three functional ports: (a) measurement scenario, (b) reflection coefficients, (c) transmission coefficients.

Therefore, due to the back-end's addition, the loss of total gain is about 2 dBi. While a 28 dBi estimated gain value of front-end array is made in III. A part, here the total gain of the final design is estimated to be 26 dBi, which is 2 dBi smaller than the simulated values shown in Fig. 15 (b) and Fig. 15 (c). After analysis, it is deduced that there are two main reasons for this deviation. One is the roughness of the formulas adopted in our estimation. The other reason is the small radiation efficiency used in the front-end gain estimation. Nevertheless, this essential method can be treated as an important reference in the early design process where appropriate performance allowances can be retained on the basis of estimated calculations. Measured HPBW in E plane is 5° and narrower 3° than simulation, while both simulated

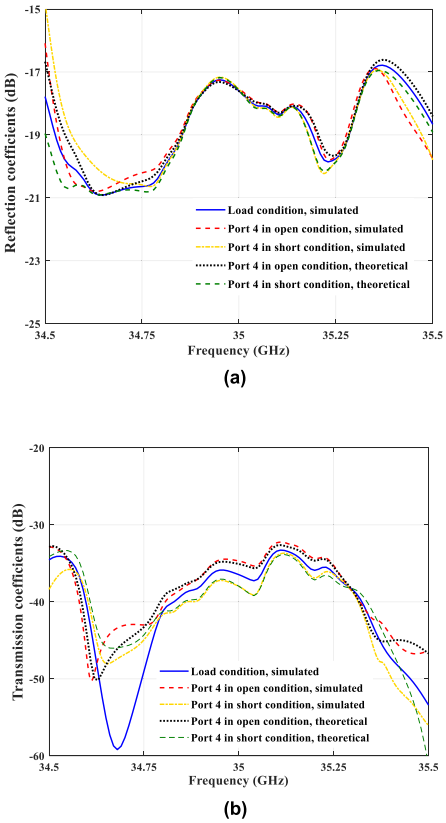

FIGURE 14. S-parameters on port 2 under the port 4's open and short conditions: (a) reflection coefficients of port 2, (b) transmission coefficients from port 2 to port 3.

and measured HPBW in H plane are 5.5°. The maximum FSLL in the two orthogonal cut planes reach about −24 dB and deteriorate by 6 dB and 4 dB compared with theoretical and simulated results, respectively, which is mainly due to the interference in the test environment and the antenna's manufacturing errors. For difference patterns, −30 dB null depth is achieved in both E and H planes' measured patterns. The measured one-sided HPBW in E plane is narrower 3° than simulation, which also appears in the sum patterns. Although there are slight deviations, the measured patterns show high consistencies with the corresponding simulated patterns, especially in the main lobe domain. In addition, measured peak cross-polarization level is −23 dB and proves good linear polarization of the proposed design.

In addition, for the far field measurement scenario in Fig. 15 (a), its set-ups are shown in Fig. 16. The link-budget is briefly analyzed as follows. First, the output continuous wave (CW) signal's power P_s from VNA at 35 GHz is set to 1 dBm. Line losses L_t from the power amplifier to the standard horn as transmitting antenna is taken as 1 dB. Both gain of RF power amplifier G_A and horn G_t are 20 dB. Second, for the free space link, its losses can be calculated according to the Friis transmission equation. When the transceiver distance is 8 m, the link losses L_f is about 81 dB. Third, at receiving end, line losses L_r from the antenna under test (AUT) to

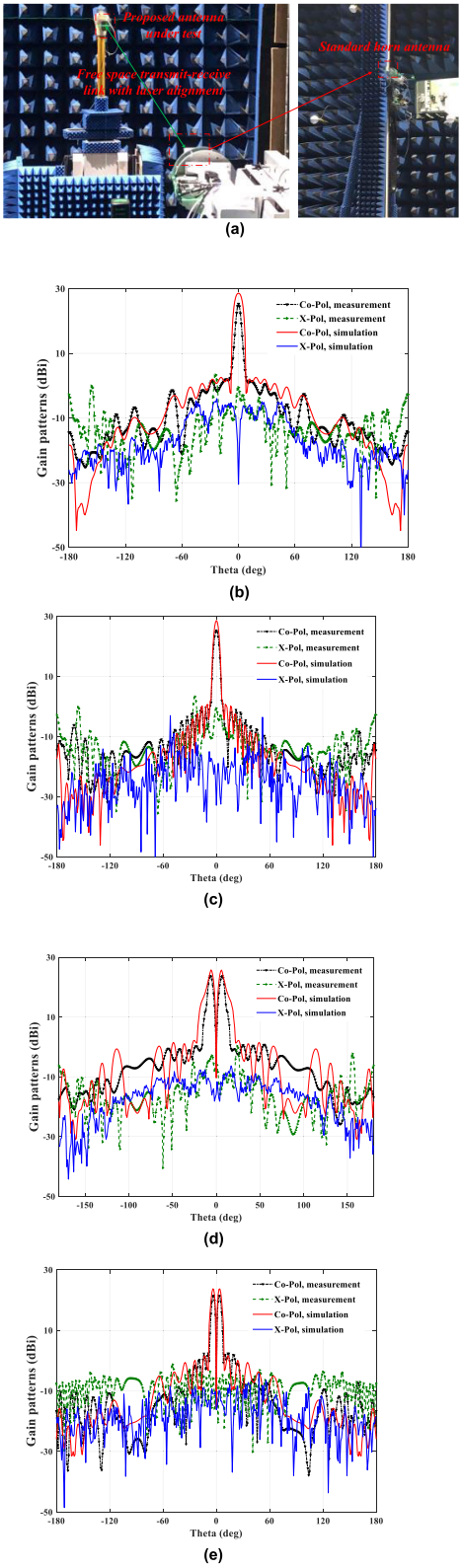

FIGURE 15. Simulated and measured co- and cross- polarization gain patterns of the designed antenna: (a) measurement scenario, (b) sum patterns in the E-plane, (c) sum patterns in the H-plane, (d) difference patterns in the E-plane, (e) difference patterns in the H-plane.

the low noise amplifier (LNA) is taken as 2 dB, and the LNA's gain G_l is 20 dB. Combined with the measured results

TABLE 4. Comparison between this work and previous works.

Ref.	Structure			Performance					
	Front-and	Back-end	Size (mm)	Working band	Gain (dBi)	FSLL (dB)	FBR (dB)	Null depth (dB)	Cross-polarization level (dB)
[9]	2 × 2 patches array	Microstrip comparator	50 × 42 length × width	X	12.5	-19	30	-27	-20
[10]	21 × 4 parallel feed patches array	Microstrip comparator with air gap	240 diameters	X	24.4	-15	Not given	-35	Not given
[11]	4 × 4 patches array	Microstrip comparator with parallel feed coupling patch array	210 × 210 length × width	C	18.4	-12	Not given	-28	Not given
[12]	19 × 4 patches array	Microstrip comparator with parallel feed network	200 diameters	X	20.45	-20	20	-22	Not given
[13]	64 × 4 parallel feed patches array	Coplanar microstrip comparator	280 × 260 length × width	Ku	24.5	-16	Not given	-30	Not given
[14]	Radial waveguide slot array	Microstrip comparator	80 diameters	X	18.1	-14.9	Not given	-31	-25
[15]	SIW slot array	SIW comparator	130 × 125 length × width	W	21.29	-6	Not given	-45.81	Not given
[16]	SIW slot array	Microstrip parallel feed network and comparator	114 × 60 length × width	X	16.4	-11	31	-33.8	Not given
[21]	6-port 3 × 3 series feed patches array	6 side-fed SMA coaxial connectors	80 × 80 length × width	X	12.2	-25.4	31	N/A	-30
[23]	1 × 10 Chebyshev weighted series feed patches array	Center back-fed coaxial probe	100 × 15 length × width	K	17.4	-26.3	37	N/A	-30
[24]	Combination of X-band four quadrant 6 × 6 patches array and K-band cross 2 × 10 patches array	Side-fed coaxial connectors and center back-fed coaxial probes	150 × 150 length × width	X/K	24/17.2	-15/-26	54/37	N/A	-54/-30
This work	80 × 4 Taylor weighted series feed patches array	Stripline comparator	145 × 135 length × width	Ka	25.3	-24	40	-30	-23

in Fig. 15, it can be seen that when the measured receiving antenna is facing the horn and back to the horn, the difference in VNA's receiving power P_r is about 40 dB. For the KEYSIGHT-N5225A PNA vector network analyzer used in our test, its system dynamic range can be qualified for requirements.

3) COMPARISONS WITH OTHER DESIGNS

Comprehensive performance comparisons between this design and some other PCB-based array antenna structures are summarized in Table 4. Compared with homogeneous monopulse microstrip array designs in [9]–[13], this structure adopts series-fed radiation array with symmetrical four

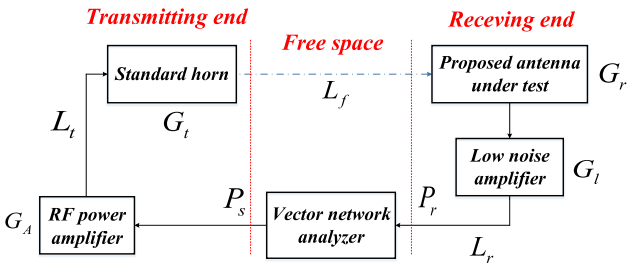

FIGURE 16. Far field pattern measurement set-up.

quadrant layout, hence the array configuration is greatly simplified and complicated large scale feeding networks are not required as in [10] and [12], [13]. The backward radiation issue resulted from the microstrip line exposed on the PCB bottom surface in [9]–[12] and [14] is effectively solved by using the stripline back-end. Because the stripline's bottom side is fully coated by a copper ground, the backward radiation is significantly suppressed. In addition, high flatness of the proposed antenna can be achieved by integrating with duralumin plate without serious back lobe deterioration due to the exposed back-end network as in [9]–[12] and [14]. As compared with the large scale SIW feed lines adopted in [15], the processing difficulty and cost are greatly reduced.

Meanwhile, this design does have some shortcomings. First, only 8.2% aperture efficiency is obtained according to the formula given in [17]. In order to improve the aperture efficiency, further works on miniaturization need to be conducted, such as adopting a compact monopulse comparator as in [9], [10]. Also, the relative bandwidth of the proposed antenna reaches only 2.8%, which still has some room for improvement. For example, a method of loading parasitic patches as in [10] can be used to broaden the bandwidth. Notably, at MMW band, there are larger Joule losses and dispersion effects from the cropper and substrate, which shows that the substrate's dielectric constant and microstrip line's characteristic impedance turn to complex values and change with frequency. Yet our proposed antenna is designed under perfect conductor and dielectric conditions. Undoubtedly, these undesirable factors will cause inaccuracy in design procedures and deviations between simulated and theoretical work. Moreover, the patches' surface roughness also plays important role in causing conductor losses. Considering the above aspects, in order to reduce the dispersion effects and dielectric losses in MMW applications, thinner substrate with low dielectric constant can be used, such as the emerging ceramic substrate technology. While for reducing the conductor losses, a little thicker copper layer with smooth surface can be used to realize better transmission performance and effectively suppress the spurious radiations from the feed network at this high frequency.

V. CONCLUSION

This study proposes a highly directional 2D series-fed monopulse microstrip array antenna. This antenna is designed for application as a ground-based monopulse radar for airspace detection purpose, where the abilities of anti-interference in the near ground clutter environments and distinguishing the false targets are strongly needed.

The main innovation of our work is the stripline feeding technique. Through this strategy, the problem of high design difficulty, side lobe and cross polarization in in some single-layer PCB design such as [13] and [15] listed in the references part is improved. The gain and back lobe deterioration drawbacks caused by the exposed comparator network, such as in [10] and [12] listed in the references, are effectively solved.

The structure is composed of symmetrical four quadrant radiation array and a stripline monopulse comparator with two segments. The design procedure is greatly simplified. Tapering patch width and loading impedance transformer methods are respectively used to realize Taylor synthesized sum patterns in E plane and H plane. The ideal radiation performances of low FSLL and low FBR are easily obtained due to the separated four quadrant front-end array and compact stripline comparator back-end that are adopted in this design. Good agreement is shown between the measured and simulated gain patterns. The measured S-parameters can satisfy the system requirements across the 34.5 GHz to 35.5 GHz working band. All these reasonable results prove the feasibility and promising prospects of the antenna in Ka-band precision tracking radar applications.

REFERENCES

[1] J. Hatch, A. Topak, R. Schnabel, T. Zwick, R. Weigel, and C. Waldschmidt, "Millimeter-wave technology for automotive radar sensors in the 77 GHz frequency band," *IEEE Trans. Microw. Theory Techn.*, vol. 60, no. 3, pp. 845–860, Mar. 2012.

[2] C. Waldschmidt, J. Hasch, and W. Menzel, "Automotive radar—From first efforts to future systems," *IEEE J. Microw.*, vol. 1, no. 1, pp. 135–148, Jan. 2021.

[3] P. Almorox-Gonzalez, J.-T. Gonzalez-Partida, M. Burgos-Garcia, B. P. Dorta-Naranjo, and J. Gismero, "Millimeter-wave sensor with FMICW capabilities for medium-range high-resolution radars," *IEEE Trans. Microw. Theory Techn.*, vol. 57, no. 6, pp. 1479–1486, Jun. 2009.

[4] J. Klare, O. Biallawons, and D. Cerutti-Maori, "UAV detection with MIMO radar," presented at the 18th Int. Radar. Symp. (IRS), Prague, Czech Republic, Jun. 2017.

[5] P. N. Melezhik, Y. B. Sidorenko, S. A. Provalov, V. B. Razskazovskiy, N. G. Reznichenko, V. A. Zuykov, M. G. Balan, A. V. Varavin, M. V. Kolisnichenko, and Y. N. Mus'kin, "Ka-band radar sensor with selection of moving targets for airport surface monitoring," presented at the 11th Int. Radar. Symp. (IRS), Vilnius, Lithuania, Jun. 2010.

[6] G. El-Arnauti, O. Saalmann, and A. R. Brenner, "Ultra-high resolution airborne experiments with a new Ka-band SAR sensor," in *Proc. 14th Eur. Radar Conf. (EURAD)*, Nuremberg, Germany, Oct. 2017, pp. 409–412.

[7] C. C. Ling and G. M. Rebeiz, "94 GHz integrated horn monopulse antennas," *IEEE Trans. Antennas Propag.*, vol. 40, no. 8, pp. 981–984, Aug. 1992.

[8] R. R. Kinsey, "An edge-slotted waveguide array with dual-plane monopulse," *IEEE Trans. Antennas Propag.*, vol. 47, no. 3, pp. 474–481, Mar. 1999.

[9] S. A. Khatami, J. Meiguni, A. A.-E. Elahi, and P. Rezaei, "Compact via-coupling fed monopulse antenna with orthogonal tracking capability in radiation pattern," *IEEE Antennas Wireless Propag. Lett.*, vol. 19, no. 8, pp. 1443–1446, Aug. 2020.

[10] H. Kumar and G. Kumar, "Broadband monopulse microstrip antenna array for X-band monopulse tracking," *IET Microw., Antennas Propag.*, vol. 12, no. 13, pp. 2109–2114, Oct. 2018.

[11] Z. W. Yu, G. M. Wang, and C. X. Zhang, "A broadband planar monopulse antenna array of C-band," *IEEE Antennas Wireless Propag. Lett.*, vol. 8, pp. 1325–1328, 2009.
[12] M. Atamanesh, B. A. Arand, and A. Zahedi, "Wideband microstrip antenna array with simultaneously low sidelobe level in both sum and difference patterns," *IET Microw., Antennas Propag.*, vol. 12, no. 5, pp. 820–825, Apr. 2018.
[13] H. Wang, D.-G. Fang, and X. G. Chen, "A compact single layer monopulse microstrip antenna array," *IEEE Trans. Antennas Propag.*, vol. 54, no. 2, pp. 503–509, Feb. 2006.
[14] J. Aliasgari and Z. Atlasbaf, "A novel compact monopulse parallel-plate slot array antenna," *IEEE Antennas Wireless Propag. Lett.*, vol. 15, pp. 762–765, 2016.
[15] Y. J. Cheng, W. Hong, and K. Wu, "94 GHz substrate integrated monopulse antenna array," *IEEE Trans. Antennas Propag.*, vol. 60, no. 1, pp. 121–129, Jan. 2012.
[16] W. Li, S. Liu, J. Deng, Z. Hu, and Z. Zhou, "A compact SIW monopulse antenna array based on microstrip feed," *IEEE Antennas Wireless Propag. Lett.*, vol. 20, no. 1, pp. 93–97, Jan. 2021.
[17] T. Yang, Z. Zhao, D. Yang, X. Liu, and Q.-H. Liu, "A single-layer SIW slots array monopulse antenna excited by a dual-mode resonator," *IEEE Access*, vol. 7, pp. 131282–131288, 2019.
[18] W. Menzel and A. Moebius, "Antenna concepts for millimeter-wave automotive radar sensors," *Proc. IEEE*, vol. 100, no. 7, pp. 2372–2379, Jul. 2012.
[19] J. Xu, W. Hong, H. Zhang, G. Wang, Y. Yu, and Z. H. Jiang, "An array antenna for both long- and medium-range 77 GHz automotive radar applications," *IEEE Trans. Antennas Propag.*, vol. 65, no. 12, pp. 7207–7216, Dec. 2017.
[20] J. Zhao, L. Zou, R. Jiang, X. Wang, and H. Gao, "Hybird antenna arrays with high angular resolution for 77 GHz automotive radars," *IEICE Electron. Exp.*, vol. 17, no. 2, pp. 1–6, Dec. 2019.
[21] V. K. Kothapudi and V. Kumar, "A 6-port two-dimensional 3×3 series-fed planar array antenna for dual-polarized X-band airborne synthetic aperture radar applications," *IEEE Access*, vol. 6, pp. 12001–12007, 2018.
[22] V. K. Kothapudi and V. Kumar, "Compact 1×2 and 2×2 dual polarized series-fed antenna array for X-band airborne synthetic aperture radar applications," *J. Electromagn. Eng. Sci.*, vol. 18, no. 2, pp. 117–128, Apr. 2018.
[23] V. K. Kothapudi and V. Kumar, "SFCFOS uniform and Chebyshev amplitude distribution linear array antenna for K-band applications," *J. Electromagn. Eng. Sci.*, vol. 19, no. 1, pp. 64–70, Jan. 2019.
[24] V. K. Kothapudi and V. Kumar, "Hybrid-fed shared aperture antenna array for X/K-band airborne synthetic aperture radar applications," *IET Microw., Antennas Propag.*, vol. 15, no. 1, pp. 93–102, Jan. 2021.
[25] H. Kumar and G. Kumar, "Monopulse comparators," *IEEE Microw. Mag.*, vol. 20, no. 3, pp. 13–100, Mar. 2019.
[26] Y. Huang and K. Boyle, "Popular antennas," in *Antennas: From Theory to Practice*, 1st ed. London, U.K.: Wiley, 2008, ch. 5, sec. 2, pp. 184–189.
[27] C. A. Balanis, "Fundamental parameters and figures-of-merit of antennas," in *Antenna Theory: Analysis and Design*, 4th ed. Hoboken, NJ, USA: Wiley, 2015, ch. 2, sec. 7, p. 48.
[28] D. M. Pozar, "Microwave network analysis," in *Microwave Engineering*, 4th ed. Hoboken, NJ, USA: Wiley, 2012, ch. 4, sec. 3, p. 183.

LE ZOU received the M.S. degree in electronic science and technology from the Beijing University of Posts and Telecommunications, Beijing, China, in 2017. He is currently pursuing the Ph.D. degree with the School of Information and Electronics, Beijing Institute of Technology.

His research interests include antenna theory and designs, millimeter-wave radar, and terahertz optics.

XUETIAN WANG received the B.E. and Ph.D. degrees in electronic engineering from the Beijing Institute of Technology, Beijing, China, in 1986 and 2002, respectively.

He is currently a Full Professor with the School of Information and Electronics, Beijing Institute of Technology. His current research interests include antenna theory and applications, millimeter-wave imaging, EMC, and terahertz radar.

JIAWEI ZANG (Member, IEEE) received the Ph.D. degree in electrical engineering from the Beijing Institute of Technology, Beijing, China, in 2019.

He is currently a Researcher with the China Academy of Information and Communications Technology. His research interests include antennas, filters, and nonreciprocal components.